Quadrature-Free Implementation of a Discontinuous Galerkin Global Shallow-Water Model via Flux Correction Procedure

RAMACHANDRAN D. NAIR

Institute for Mathematics Applied to Geosciences, National Center for Atmospheric Research, Boulder, Colorado*

(Manuscript received 31 May 2014, in final form 30 November 2014)

ABSTRACT

The discontinuous Galerkin (DG) discretization relies on an integral (weak) formulation of the hyperbolic conservation law, which leads to the evaluation of several surface and line integrals for multidimensional problems. An alternative formulation of the DG method is possible under the flux reconstruction (FR) framework, where the equations are solved in differential form and the discretization is free from quadrature rules, resulting in computationally efficient algorithms. The author has implemented a quadrature-free form of the nodal DG method based on the FR approach combined with spectral differencing (SD), in a shallow-water (SW) model employing cubed-sphere geometry. The performance of the SD model is compared with the regular nodal DG variant of the SW model using several benchmark tests, including a viscous test case. A positivity-preserving local filter is tested for SD advection that removes spurious oscillations while being conservative and accurate. In this implementation, the SD formulation is found to be 18% faster than the DG method for inviscid SW tests cases and 24% faster for the viscous case. The results obtained by the SD formulation are on par with the regular nodal DG formulation in terms of accuracy and convergence.

1. Introduction

Among the emerging numerical methods for spatial discretization, the discontinuous Galerkin (DG) method (Cockburn 1997) is considered to be a prominent candidate for atmospheric modeling (Nair et al. 2011) because of multiple computationally attractive features such as conservation, high-order accuracy, and excellent parallel efficiency. The DG methods employ an integral (weak) formulation of the hyperbolic conservation law in the solution process. This leads to the evaluation of several surface and line integrals in the discretization of multidimensional problems, and results in a robust but computationally expensive scheme. In an effort to improve the computational efficiency of the DG method, Atkins and Shu (1998) introduced a quadrature-free form. Another method, the spectral difference scheme (Kopriva and Kolias 1996; Liang et al. 2013), employs the differential form of the conservation law and avoids surface and line integrals altogether in the discretization, while being accurate.

Recently, Huynh (2007) introduced a new approach to high-order accuracy called flux reconstruction (FR), where equations are solved in differential form. An interesting feature of the FR approach is that it unifies several existing element-based high-order methods such as DG, spectral difference, and spectral volume methods into a common framework. The discontinuous fluxes at the element edges are corrected by *correction functions*, which maintain flux continuity across the element edges. Individual schemes in the framework can be recovered by choosing the appropriate correction function (Huynh 2007). The FR framework further can be extended for diffusion problems where several existing schemes, including those used for the DG method, are reformulated or simplified (Huynh 2009). The subtle difference among the various schemes is dependent only on the choice of these correction functions. This is an active area of research, in which new variants of FR scheme such as the "energy stable FR" (Allaneau and Jameson 2011), and more sophisticated reconstruction functions (Huynh 2014) with computationally attractive properties have been recently introduced.

A nonstaggered version of spectral difference method using the FR approach renamed as the correction

* The National Center for Atmospheric Research is sponsored by the National Science Foundation.

Corresponding author address: R. D. Nair, Computational and Information System Laboratory, National Center for Atmospheric Research, 1850 Table Mesa Dr., Boulder, CO 80305.
E-mail: rnair@ucar.edu

DOI: 10.1175/MWR-D-14-00174.1

procedure via reconstruction (CPR) approach introduced for the Navier–Stokes equations (Gao et al. 2013). The quadrature-free nodal DG method can be obtained by the FR procedure (see Gao et al. 2013), a potential advantage of this approach being the computational efficiency, which stems from the differential formulation of the governing equations. May (2011) showed that the quadrature-free nodal DG method and the collocation-based (unstaggered) spectral difference method are equivalent under certain conditions. Recently, De Grazia et al. (2014) demonstrated the connection between a nodal DG scheme and the corresponding FR formulation using the two-dimensional (2D) advection equation, and compared the computational efficiency. In this paper we describe the implementation of the quadrature-free DG based on the FR method [hereafter this is referred to as the FR based spectral differencing (SD) method] for the shallow-water (SW) equations on the cubed sphere, and compare its performance with a regular nodal DG method employing the integral (weak) formulation (Bao et al. 2014). The SW test case also includes a viscous flow test where the viscous fluxes (diffusion terms) are discretized with the SD approach. In addition, a positivity-preserving filter is tested for the SD advection using a standard benchmark test.

The remainder of the paper is organized as follows. The SW model, nodal DG, and SD approaches are presented in section 2. Section 3 describes numerical experiments, followed by a summary in section 4.

2. Shallow-water model on the cubed sphere

Various formulations of the SW equations on the cubed sphere using the nodal DG discretization can be found in Bao et al. (2014), Nair (2009), Nair et al. (2005), and Giraldo et al. (2002). The cubed-sphere formulation consists of mapping a cube onto a sphere by the central (gnomonic) projection, which results in nonorthogonal curvilinear spherical domain (Sadourny 1972). The computational domain $\mathcal{D}$ can be expressed in terms of local coordinates $[x(\lambda, \theta), y(\lambda, \theta)]$ on each face of the cube such that $-\pi/4 \le x, y \le \pi/4$, and (λ, θ) are the regular spherical longitude–latitude coordinates of a sphere with radius R. The metric tensor G_{ij} associated with the transformation is

$$G_{ij} = \frac{R^2}{\rho^4 \cos^2 x \cos^2 y} \begin{pmatrix} 1+\tan^2 x & -\tan x \tan y \\ -\tan x \tan y & 1+\tan^2 y \end{pmatrix}, \quad (1)$$

where $\imath, \jmath \in \{1, 2\}$ and $\rho^2 = 1 + \tan^2 x + \tan^2 y$. The Jacobian of the central mapping (the metric term) is $\sqrt{G} = [\det(G_{ij})]^{1/2}$. For brevity, we only outline the SW equations here. Details of the cubed-sphere mapping and SW formulation can be found in Nair et al. (2005).

The SW equations are treated in tensor form with covariant ($u_\imath$) and contravariant ($u^\imath$) wind vectors, which are related through $u_\imath = G_{\imath\jmath} u^\jmath$, $u^\imath = G^{\imath\jmath} u_\jmath$, and $G^{\imath\jmath} = G_{\imath\jmath}^{-1}$. The inviscid SW equations can be written in terms of the fluid depth h as

$$\frac{\partial}{\partial t}\mathbf{U} + \frac{\partial}{\partial x}\mathbf{F}_1(\mathbf{U}) + \frac{\partial}{\partial y}\mathbf{F}_2(\mathbf{U}) = \mathbf{S}(\mathbf{U}), \quad (2)$$

where $\mathbf{U} = (u_1, u_2, \sqrt{G}h)^{\mathrm{T}}$ is the state vector combined with Jacobian $\sqrt{G}$. The terms $\mathbf{F}_1$ and $\mathbf{F}_2$ are flux vectors and $\mathbf{S}$ is the source vector, defined as follows:

$$\mathbf{F}_1 = (E, 0, \sqrt{G}hu^1)^{\mathrm{T}}, \quad \mathbf{F}_2 = (E, 0, \sqrt{G}hu^2)^{\mathrm{T}},$$
$$\mathbf{S}(\mathbf{U}) = [\sqrt{G}u^2(f+\zeta), -\sqrt{G}u^1(f+\zeta), 0]^{\mathrm{T}},$$

where $E = \Phi + (1/2)(u_1 u^1 + u_2 u^2)$ is the energy term, $\Phi = g(h + h_s)$ is the geopotential height, h_s is the surface topography, and g is the gravitational acceleration. The source vector contains the relative vorticity $\zeta = (\partial u^2/\partial x - \partial u^1/\partial y)/\sqrt{G}$ and the Coriolis parameter f.

A viscous SW model contains additional diffusive fluxes on the right-hand side of (2). For simplicity, we consider the viscous flux vector to be defined in terms of a scalar viscosity combined with a constant diffusion coefficient ν, which may be written as (Nair 2009), $\mathbf{D}(\mathbf{U}) = (\nu\sqrt{G}\nabla_s^2 u_1, \nu\sqrt{G}\nabla_s^2 u_2, 0)^{\mathrm{T}}$, where ∇_s^2 denotes the spherical Laplacian in cubed-sphere coordinates. For an arbitrary variable U, the Laplacian terms in $\mathbf{D}(\mathbf{U})$ can be written in the following explicit form:

$$\sqrt{G}\nabla_s^2 U \equiv \frac{\partial}{\partial x}\left(\sqrt{G}G^{11}\frac{\partial U}{\partial x} + \sqrt{G}G^{12}\frac{\partial U}{\partial y}\right) + \frac{\partial}{\partial y}\left(\sqrt{G}G^{21}\frac{\partial U}{\partial x} + \sqrt{G}G^{22}\frac{\partial U}{\partial y}\right). \quad (3)$$

a. Nodal DG discretization

For simplicity, we consider a scalar component of the system in (2) on the computational domain $\mathcal{D}$, which consists of $N_e \times N_e \times 6$ elements, where N_e is the number of elements in x or y direction:

$$\frac{\partial U}{\partial t} + \frac{\partial F_1(U)}{\partial x} + \frac{\partial F_2(U)}{\partial y} \equiv \frac{\partial U}{\partial t} + \nabla \cdot \mathbf{F}(U) = S(U) \text{ in } \mathcal{D} \times (0, T], \quad (4)$$

where $\mathbf{F} = (F_1, F_2)$, $\nabla = (\partial/\partial x, \partial/\partial y)$, and T is a prescribed time. Without loss of generality, we may describe the DG discretization on a generic element Ω_{ij} in $\mathcal{D}$ with the boundary Γ_{ij}. Let $\mathcal{V}_h$ be a vector space of polynomials of degree up to N, and let U_h be the

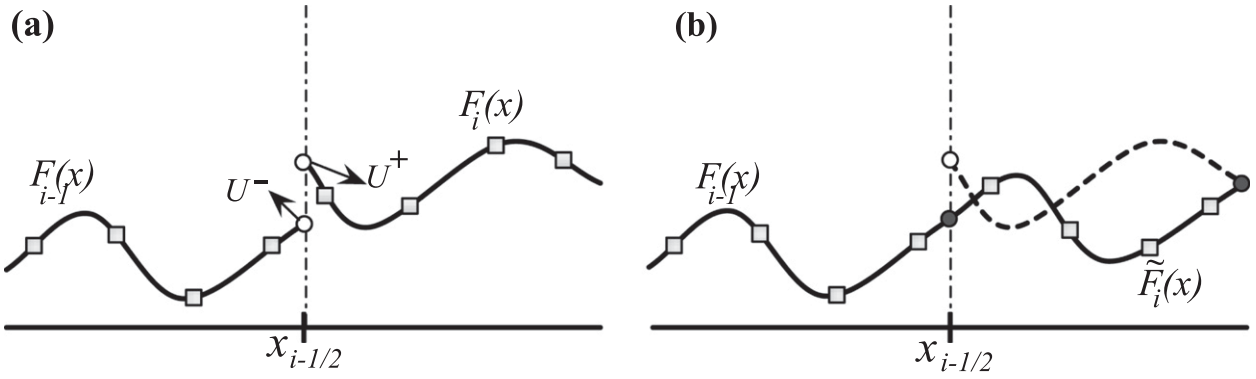

FIG. 1. A schematic diagram showing the flux reconstruction (FR) procedure where squares indicate solution points. (a) Discontinuous state of the solutions U^- and U^+ on the left and right of the element interface $x_{i-1/2}$, respectively, are marked as open circles. Piecewise polynomials $F_{i-1}(x)$ and $F_i(x)$ represent the discontinuous flux functions, which belong to the adjacent elements from the left and right side of $x_{i-1/2}$, respectively. (b) $\tilde{F}_i(x)$ is the reconstructed continuous flux function by FR procedure, which has the upwind flux value (black dot) at the element interface.

approximate solution for U in $\mathcal{V}_h$. Then the weak Galerkin formulation of the problem can be obtained by multiplying (4) by a test function $\varphi_h \in \mathcal{V}_h$, and integrating by parts over Ω_{ij} (Cockburn 1997):

$$\frac{d}{dt}\int_{\Omega_{ij}} U_h\varphi_h\, d\Omega - \int_{\Omega_{ij}} \mathbf{F}(U_h)\cdot\nabla\varphi_h\, d\Omega + \int_{\Gamma_{ij}} \hat{\mathbf{F}}\cdot\mathbf{n}\varphi_h\, d\Gamma = \int_{\Omega_{ij}} S(U_h)\varphi_h\, d\Omega, \quad \forall \quad \Omega_{ij}\in\mathcal{D}, \tag{5}$$

where $\mathbf{n}$ is the outward-drawn unit normal vector on Γ_{ij}, and $\hat{\mathbf{F}}$ is the numerical flux. We use the local Lax–Friedrichs (Rusanov) numerical flux,

$$\hat{\mathbf{F}}(U_h) = \frac{1}{2}\{[\mathbf{F}(U_h^-) + \mathbf{F}(U_h^+)] - \alpha_{\max}(U_h^+ - U_h^-)\mathbf{n}\}, \tag{6}$$

where $\alpha_{\max}$ is the maximum of the eigenvalues of the flux Jacobian for the SW system, which are defined in x and y direction as (Nair et al. 2005)

$$\alpha_{\max}|_x = \max(|u^1| + \sqrt{G^{11}gh}),$$
$$\alpha_{\max}|_y = \max(|u^2| + \sqrt{G^{22}gh}),$$

where U_h^- and U_h^+ are values of U_h, respectively, at the interface (Fig. 1a) along the boundary Γ_{ij}.

Solving the weak form in (5) involves mapping the nonoverlapping rectangular elements Ω_{ij} in the computational domain $\mathcal{D}$ to a standard element $\hat{\Omega} = (-1,1)^2$. The grid spacings are defined to be $\Delta x_i = (x_{i+1/2} - x_{i-1/2})$ and $\Delta y_j = (y_{j+1/2} - y_{j-1/2})$, such that $|\Omega_{ij}| = \Delta x_i \Delta y_j$. Let $x_i = (x_{i+1/2} + x_{i-1/2})/2$ and $y_j = (y_{j+1/2} + y_{j-1/2})/2$, then the mapping $\Omega_{ij} \to \hat{\Omega}$ can be established through the local coordinates ξ, $\eta \in [-1, 1]$ as follows:

$$\xi = \frac{2(x-x_i)}{\Delta x_i} \Rightarrow \frac{\partial}{\partial x} = \frac{2}{\Delta x_i}\frac{\partial}{\partial \xi}; \quad \eta = \frac{2(y-y_j)}{\Delta y_j} \Rightarrow \frac{\partial}{\partial y} = \frac{2}{\Delta y_j}\frac{\partial}{\partial \eta}. \tag{7}$$

To evaluate the integrals in (5) efficiently, an orthogonal polynomial-based basis set is usually employed. Here we adopt the nodal DG discretization, which employs the Lagrange polynomials $h_k(\xi)$, $0 \le k \le N$ (with $N+1 = N_v$ solution points), as the basis functions with roots at the Gauss–Lobatto–Legendre (GLL) quadrature points $\{\xi_k\}_{k=0}^N$ (Deville et al. 2002). The basis functions are defined by

$$h_k(\xi) = \frac{(\xi-1)(\xi+1)P_N'(\xi)}{N(N+1)P_N(\xi_k)(\xi-\xi_k)}, \tag{8}$$

where $P_N(\xi)$ is the Legendre polynomial of degree N, and the derivative of the basis function $h_k'(\xi)$ at the nodal points constructs the derivative matrix:

$$h_k'(\xi_l) = \begin{cases} \dfrac{P_N(\xi_k)}{P_N(\xi_l)}\dfrac{1}{(\xi_k-\xi_l)} & \text{if} \quad k \ne l, \\ -\dfrac{(N+1)N}{4} & \text{if} \quad k = l = 0, \\ \dfrac{(N+1)N}{4} & \text{if} \quad k = l = N, \\ 0 & \text{otherwise}, \end{cases} \tag{9}$$

required for the collocation differentiation.

The approximate solution U_h and test function φ_h can be expanded in terms of a tensor product of the Lagrange basis functions, and in the case of U_h:

$$U_h(\xi,\eta) = \sum_{k=0}^{N}\sum_{l=0}^{N} U_h(\xi_k,\eta_l)h_k(\xi)h_l(\eta). \tag{10}$$

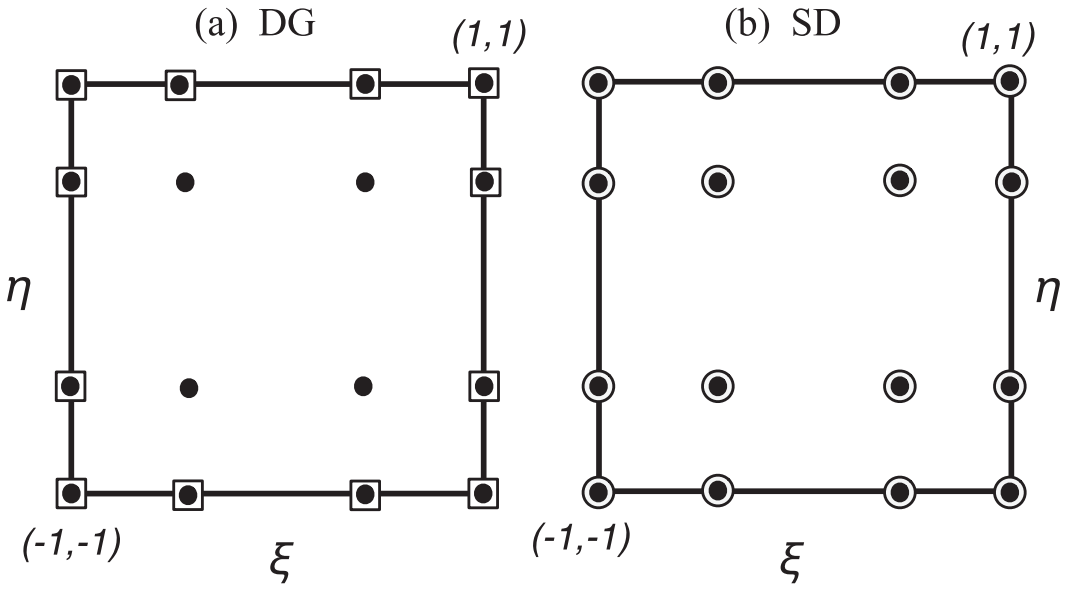

FIG. 2. The GLL quadrature stencils used for (a) the DG and (b) SD models on the reference element $[-1, 1]^2$, with 4×4 points. The solution points are marked by black dots on both stencils. Squares with black dots on the edges of the DG stencil indicate flux points on which flux (line) integrals are computed. Circles with black dots on the SD stencil indicate the flux points, which coincide with the solution points, where the flux derivatives are computed.

Figure 2 shows a GLL quadrature grid with 4×4 points. Substitution of U_h and φ_h in (5) simplifies to an ordinary differential equation (ODE) in time $dU_h/dt = L(U_h)$, where L denotes the nodal DG spatial discretization. The details of the solution procedure are given in Nair et al. (2011), and will not be further discussed herein.

b. *The flux reconstruction (correction) procedure*

The differential form of (4) can be directly solved by employing a collocation-based spectral difference method in the FR framework (Gao et al. 2013), without considering the integral form in (5). In particular, we are interested in the *flux-reconstructed* spectral difference (SD) scheme (i.e., quadrature-free nodal DG method), referred to as the SD method. A nice feature of the SD scheme is that, for a given number of solution points (ξ_i, η_j), it employs the same GLL grid as that used for the nodal DG discretization (see Fig. 2). This makes the SD implementation relatively easy in the existing nodal DG model, by avoiding the need to change the grid or data structure. Nevertheless, the numerical operations for the DG and SD schemes on the GLL grid are different. The major difference is that the SD scheme directly discretizes the differential form of the partial differential equation (PDE) and does not rely on integrals, which leads to efficient implementation and computational savings.

Since the flux correction is done in a 1D manner, it is convenient to explain the basic properties of the SD method using a simple 1D conservation law given by $\partial U_i/\partial t + \partial F_i(x)/\partial x = 0$, on the ith element $I = [x_{i-1/2}, x_{i+1/2}]$, where U_i is represented as a polynomial of degree N, with $N_v = N + 1$ solution points on I. The flux correction procedure (Huynh 2007) consists of introducing a new flux function, $\tilde{F}_i(x)$, which is a degree N_v polynomial (i.e., one degree higher than the solution polynomial U_i). Furthermore, $\tilde{F}_i(x)$ approximates $F_i(x)$ on the element and takes the common value $\hat{F}_i$ [i.e., the upwind flux in (6)] at the element edges $x_{i\pm1/2}$ (see Fig. 1). Thus, the reconstructed flux function $\tilde{F}_i(x)$ can be expressed as follows:

$$\tilde{F}_i(x) = F_i(x) + [\hat{F}_{i-1/2} - F(x_{i-1/2})]\mathcal{G}_L(x) + [\hat{F}_{i+1/2} - F(x_{i+1/2})]\mathcal{G}_R(x), \tag{11}$$

where $\mathcal{G}_L$ and $\mathcal{G}_R$ are the left and right correction functions, respectively, defined by N_v-degree polynomials. At the element edges these functions are designed to satisfy the following properties: $\mathcal{G}_L(x_{i-1/2}) = 1, \mathcal{G}_L(x_{i+1/2}) = 0$; for the right correction function $\mathcal{G}_R(x_{i-1/2}) = 0, \mathcal{G}_R(x_{i+1/2}) = 1$. Note that the reconstruction functions essentially maintain the continuity of the fluxes at the element edges. Now the 1D conservation law with the reconstructed flux in (11) can be written as follows:

$$\frac{\partial U_{i,k}}{\partial t} + \frac{\partial F_{i,k}}{\partial x} + [\hat{F}_{i-1/2} - F(x_{i-1/2})]\mathcal{G}'_L(x_{i,k}) + [\hat{F}_{i+1/2} - F(x_{i+1/2})]\mathcal{G}'_R(x_{i,k}) = 0, \tag{12}$$

where $k = 0, 1, \ldots, N$. The choice of correction functions is very crucial, for the SD method these functions

are written in terms of Radau polynomials [for details see Huynh (2007)].

c. FR versus DG formulation

Although the FR and DG methods are formulated in differential and integral forms respectively, they are closely related. Huynh (2007) showed that the FR approach using the "g_{DG}" correction function is identical to the standard DG weak formulation in the 1D case. A more rigorous proof is given in Gao et al. (2013), based on the classical "lifting operator" concept as used in Bassi and Rebay (1997). If we combine the second and third integral terms on the left-hand side of the weak form in (5), and apply Green's method, we obtain

$$-\int_{\Omega_{ij}} \mathbf{F}(U_h)\cdot\nabla\varphi_h\, d\Omega + \int_{\Gamma_{ij}} \hat{\mathbf{F}}\cdot\mathbf{n}\varphi_h\, d\Gamma$$
$$= \int_{\Omega_{ij}} \nabla\cdot\mathbf{F}(U_h)\varphi_h\, d\Omega + \int_{\Omega_{ij}} (\hat{\mathbf{F}}-\mathbf{F})\cdot\mathbf{n}\varphi_h\, d\Gamma \qquad (13)$$

$$= \int_{\Omega_{ij}} [\nabla\cdot\mathbf{F}(U_h)+\delta_h]\varphi_h\, d\Omega, \qquad (14)$$

where δ_h is the so-called lifting function, such that

$$\int_{\Omega_{ij}} \delta_h\varphi_h\, d\Omega = \int_{\Omega_{ij}} (\hat{\mathbf{F}}-\mathbf{F})\cdot\mathbf{n}\varphi_h\, d\Omega. \qquad (15)$$

Substituting (14) in (5) and simplifying yields the following differential form (see Gao et al. 2013):

$$\frac{\partial U_h}{\partial t} + \nabla\cdot\mathbf{F}(U_h) + \delta_h = S(U_h), \qquad (16)$$

which is formally equivalent to the integral form, subject to the choice of the lifting function δ_h. A judicious choice for δ_h together with consistent polynomial approximation for the flux derivative leads to the conservative formulation of (16). For example, in the 1D case, the quantities (correction terms) in the square brackets of (12) represent δ_h. A direct derivation for establishing the relation between the DG and FR methods, in the context of the 2D advection equation, can be found in De Grazia et al. (2014). The connections and the subtle differences between FR and DG schemes are a new topic of research in high-order methods and details can be found in Allaneau and Jameson (2011), De Grazia et al. (2014), and the references therein.

The SD discretization of the differential form in (16) does not involve integral evaluation of the terms and construction of a mass matrix as in the DG formulation in (5). For practical implementation, the SD scheme seems to be particularly attractive, as there are no surface or volume integrals to be computed in multidimensional cases. This is desirable for computationally intensive application such as climate modeling.

d. Extension to 2D cases

Extending the SD scheme to the 2D case is straightforward. We consider a general rectangular element Ω with area $\Delta x\times\Delta y$, where the elemental indices are suppressed for clarity. Using the local coordinates in (7), the differential form in (4) can be written as follows:

$$\frac{\partial U(\xi,\eta)}{\partial t} + \frac{2}{\Delta x}\frac{\partial F_1(\xi,\eta)}{\partial\xi} + \frac{2}{\Delta y}\frac{\partial F_2(\xi,\eta)}{\partial\eta} = S(\xi,\eta). \qquad (17)$$

We are particularly interested in solving (17) on the GLL grid $[-1,1]^2$ with $N_v\times N_v$ points $(\xi_k,\ \eta_l)$, as shown in Fig. 2. By introducing corrected fluxes for F_1 and F_2 in (17) using the relation in (11), we get the following semidiscretized 2D SD scheme:

$$\frac{dU(\xi_k,\eta_l)}{dt} + \frac{2}{\Delta x}\frac{\partial F_1}{\partial\xi} + \frac{2}{\Delta y}\frac{\partial F_2}{\partial\eta} + \frac{2}{\Delta x}\left\{\begin{array}{l}[\hat{F}_1(-1,\eta_l)-F_1(-1,\eta_l)]\mathcal{G}_L'(\xi_k)\\ +[\hat{F}_1(1,\eta_l)-F_1(1,\eta_l)]\mathcal{G}_R'(\xi_k)\end{array}\right\} + \frac{2}{\Delta y}\{[\hat{F}_2(\xi_k,-1)$$
$$-F_2(\xi_k,-1)]\mathcal{G}_L'(\eta_l) + [\hat{F}_2(\xi_k,1)-F_2(\xi_k,1)]\mathcal{G}_R'(\eta_l)\} = S(\xi_k,\eta_l). \qquad (18)$$

For the SD scheme, the flux functions are expressed in terms of Lagrange basis functions $h_k(\xi)$ and $h_l(\eta)$. The derivatives $\partial F_1/\partial\xi$ and $\partial F_2/\partial\eta$ in (18) can be computed by the collocation differentiation using $h_k'(\xi)$ and $h_k'(\eta)$ in (9) as follows:

$$\frac{\partial F_1}{\partial\xi} = \sum_{k=0}^{N}\sum_{l=0}^{N} F_1(\xi_k,\eta_l)h_k'(\xi)h_l(\eta),$$
$$\frac{\partial F_2}{\partial\eta} = \sum_{k=0}^{N}\sum_{l=0}^{N} F_2(\xi_k,\eta_l)h_k(\xi)h_l'(\eta). \qquad (19)$$

For the current application we consider the correction function g_2 or $g_{\mathrm{Lump,Lo}}$ as defined in Huynh (2007). The explicit form of g_2 at the left interface can be defined as a weighted sum of the right Radau polynomials $R_{R,N_v} = (-1)^{N_v}(P_{N_v}-P_{N_v-1})/2$ as follows:

$$g_2 = \frac{N_v-1}{2N_v-1}R_{R,N_v} + \frac{N_v}{2N_v-1}R_{R,N_v-1}.$$

An interesting property of this function is that its derivative vanishes at all solution points except at the left

boundary of the GLL grid when evaluating $\mathcal{G}'_L$, or at the right boundary when evaluating $\mathcal{G}'_R$ [for details see Huynh (2007)]. The derivatives g_2 at the edges of the GLL grid $[-1, 1]$ are given by $\mathcal{G}'_L(-1) = -N_v(N_v - 1)/2$, $\mathcal{G}'_L(1) = 0$ and $\mathcal{G}'_R(1) = 0$, $\mathcal{G}'_R(1) = N_v(N_v - 1)/2$.

For the SW system, (18) leads to a system of ODEs, $d\mathbf{U}/dt = \mathcal{L}(\mathbf{U})$, which can be solved with explicit Runge–Kutta methods (Gottlieb et al. 2001; Nair 2009).

e. FR for diffusive fluxes

Bassi and Rebay (1997) introduced explicit diffusion (viscous flux) in the DG discretization, and later Cockburn and Shu (1998) laid a rigorous mathematical background to this approach and generalized it to the so-called local DG or LDG method. A wide body of literature is available for addressing the diffusion process in DG discretization (see Arnold et al. 2002). In this section, our focus is the implementation of the FR scheme for diffusive fluxes developed in Huynh (2009). This is based on an improved version of the Bassi and Rebay (1997) approach, known as the "BR2" scheme (a special case of the LDG method), which employs a compact computational stencil. The DG discretization of diffusive fluxes on the cubed-sphere grids introduces additional challenges due to the metric terms involved in the curvilinear Laplacian in (3). Nair (2009) implemented a version of the LDG scheme for the viscous SW model on the cubed sphere, but here we only outline the procedure.

For the viscous SW model, we consider a generic component of the momentum equation by extending (4) as follows:

$$\frac{\partial U}{\partial t} + \nabla \cdot \mathbf{F}(U) = \nu\sqrt{G}\nabla_s^2 U + S(U). \tag{20}$$

The LDG discretization on the cubed sphere involves introduction of an auxiliary variable $\mathbf{q} = \nabla U$, together with following notation to represent the curvilinear Laplacian $\nabla_s^2 U$ (Nair 2009; Bao et al. 2014):

$$\mathbf{q} = \left[\frac{\partial U}{\partial x}, \frac{\partial U}{\partial y}\right], \quad \mathbf{M} = \begin{bmatrix} \sqrt{G}G^{11} & \sqrt{G}G^{12} \\ \sqrt{G}G^{21} & \sqrt{G}G^{22} \end{bmatrix}, \quad \text{and} \quad \tilde{\mathbf{q}} = \mathbf{q}\mathbf{M}^{\mathrm{T}}.$$

The LDG discretization for (20) can be rewritten as a first-order system:

$$\mathbf{q} - \nabla U = 0, \tag{21}$$

$$\tilde{\mathbf{q}} = \mathbf{q}\mathbf{M}^{\mathrm{T}}, \quad \text{and} \tag{22}$$

$$\frac{\partial U}{\partial t} + \nabla \cdot \mathbf{F}(U) - \nu\nabla \cdot \tilde{\mathbf{q}} = S(U). \tag{23}$$

A weak formulation corresponding to the system in (21)–(23) is then constructed for approximating the diffusive fluxes [see Nair (2009) for details]. However, the FR-based discretization of diffusive fluxes employs a direct approach, which is free from integral formulation (Huynh 2009; Gao et al. 2013). To illustrate the procedure, we first use the above notation to represent the curvilinear Laplacian in (3) in the following form:

$$\sqrt{G}\nabla_s^2 U = \nabla \cdot \tilde{\mathbf{q}}. \tag{24}$$

The FR approach corrects the first ($\mathbf{q}$) and second derivative ($\nabla \cdot \tilde{\mathbf{q}}$) involved in the Laplacian in a sequential manner. We summarize the algorithm in the following steps:

- Step 1: Compute the gradient term $\mathbf{q} = (\partial U/\partial x, \partial U/\partial y)$ using collocation differentiation on GLL nodes. Compute the common solution $U^{\mathrm{com}} = (U^- + U^+)/2$ at the cell interfaces, where U^- and U^+ denote the left and right values of U at the interface, respectively.
- Step 2: Correct the gradient term $\mathbf{q}$ component-wise using the FR procedure used in the SD discretization in (12). For instance, the derivative $\partial U/\partial x$ is corrected as

$$\frac{2}{\Delta x}\left\{\frac{\partial U}{\partial \xi} + [U^{\mathrm{com}}(-1, \eta) - U(-1, \eta)]\mathcal{G}'_L(\xi) + [U^{\mathrm{com}}(1, \eta) - U(1, \eta)]\mathcal{G}'_R(\xi)\right\}.$$

  Similarly correct the $\partial U/\partial y$ term and obtain the corrected gradient $\mathbf{q}^c$. Denote $\mathbf{q}^c$ together with metric term as $\nabla Q = \mathbf{q}^c\mathbf{M}^{\mathrm{T}}$.
- Step 3: Compute the common gradient $\nabla Q^{\mathrm{com}} = (\nabla Q^- + \nabla Q^+)/2$ at the interface, using the left and right interface values of ∇Q. Using ∇Q^{com}, the second derivative corresponding to the viscous flux is corrected as described in step 2.

Note that for parallel implementation, the above algorithm requires only one communication (nearest neighbor) for each Laplacian evaluation, because of the compact computational stencil. Thus, the SD approach for diffusion can be significantly cheaper for incorporating hyperdiffusion (∇^4) in practical models.

3. Numerical experiments

We consider three benchmark tests suggested by Williamson et al. (1992, hereafter W92), for evaluating numerical schemes used in spherical SW models. We use these test cases to compare the performance of both SD and DG methods.

a. Solid-body rotation (advection) test

The first test case is the solid-body rotation test, where the initial scalar distribution is a *cosine-bell* profile, which makes a complete revolution on the sphere in

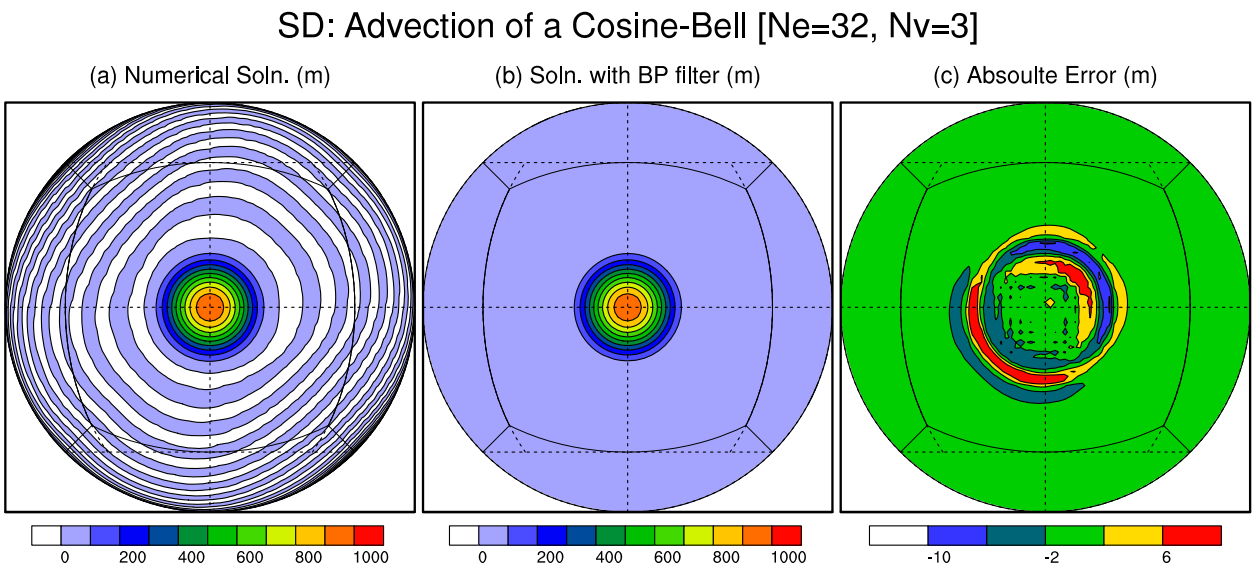

FIG. 3. Orthographic projection for the SD results with the cosine-bell advection test on a $32 \times 32 \times 6$ ($N_e = 32$) element grid where each element has 3×3 GLL quadrature points ($N_v = 3$). (a) Numerical solution after 12 model days (or one revolution) where the contours are ranging from 0 to 1000 m with an increment of 100 m. (b) As in (a), but with the bound-preserving (BP) filter. (c) Absolute error (numerical − exact solution) after 12 model days, the contour ranges from −10 to 6 with an increment of 4.

a 12-day period (W92). Although this is a linear transport problem (not involving the full SW equations), it provides a challenging test to evaluate the numerical scheme on a complex domain such as the cubed sphere. Since the exact solution is known at all times, time traces of the standard errors can be computed. The cosine-bell (U) is defined in spherical coordinates (λ, θ) as

$$U(\lambda,\theta) = \begin{cases} (h_0/2)[1+\cos(\pi r_d/r_0)] & \text{if} \quad r_d < r_0 \\ 0 & \text{if} \quad r_d \geq r_0 \end{cases}, \tag{25}$$

where r_d is the great-circle distance between (λ, θ) and the center of the cosine bell (λ_c, θ_c), $h_0 = 1000$ m is the *height* of the bell. The radius of the sphere (the earth) is $R = 6.371\,22 \times 10^6$ m and the base radius of the cosine bell is $r_0 = R/3$. The center of the cosine bell is initially positioned on the equator at $(\lambda_c, \theta_c) = (3\pi/2, 0)$. The spherical velocity components (u, v) of the nondivergent wind field are defined to be

$$u = u_0(\cos\alpha\cos\theta + \sin\alpha\cos\lambda\sin\theta), \tag{26}$$

$$v = -u_0\sin\alpha\sin\lambda, \tag{27}$$

where $u_0 = 2\pi R/(12$ days), and α is the flow orientation parameter (W92). When $\alpha = \pi/4$, the flow is along the northeast direction; as a result the cosine bell passes through four vertices and two edges of the cubed sphere to complete one revolution.

We compare the SD results with that of the multimoment finite-volume (FV) results given in Chen and Xiao (2008), which uses a method that has certain features similar to SD methods. To make a rigorous comparison, we consider a relatively low-order SD grid configuration with $32 \times 32 \times 6$ elements ($N_e = 32$) on the cubed sphere such that each element employs 3×3 GLL points or nine degrees of freedom (dof). Note that the FV computational stencil used by Chen and Xiao (2008) is very similar to the 3×3 GLL grid, moreover, both methods have the same dof per cell (element). For this test we used a standard fourth-order Runge–Kutta time integration scheme with time step $\Delta t = 2025$ s, so that 512 iterations (12 days) are required for a complete revolution. The numerical solution with the SD scheme is shown in Fig. 3a, where the height of the cosine bell has the range $[-10.1, 997.9]$ m. Zero-contour lines are included in the plot, which clearly show the oscillatory nature of the solution, which is typical of any high-order advection scheme without a limiter. The absolute error is shown in Fig. 3c. After a complete revolution, these values are $\ell_1 = 2.265 \times 10^{-2}$, $\ell_2 = 1.381 \times 10^{-2}$, and $\ell_\infty = 1.080 \times 10^{-2}$, which are smaller than the corresponding values shown in Table 4 of Chen and Xiao (2008). The corresponding DG results are virtually identical to that of the SD results; however, the SD simulation is faster because of the reduced number of inter-element (quadrature free) computations.

b. *A positivity-preserving filter for SD advection*

For atmospheric tracer transport models, the positivity preservation is considered to be a basic requirement.

For passive tracers such as water vapor, and certain chemical species, the global maximum and minimum mixing-ratio values are known in advance. To preserve the initial bounds of the numerical solutions and eliminate negative concentrations we can apply a bound-preserving (BP) filter as an additional option for the SD advection scheme. The BP filter was introduced by Zhang and Shu (2010) for DG methods, which is a local scheme with attractive features such as conservation, computational economy, and ease of implementation (Zhang and Nair 2012). Since the nodal DG and SD schemes employ the same type of stencils (Fig. 2), we extend the filter to the SD case.

Let $p_{ij}(x, y)$ be the SD solution polynomial on the cell Ω_{ij} with known (computed) cell-average $\overline{u}_{ij}$. The BP filter essentially replaces the oscillatory polynomial $p_{ij}(x, y)$ with a modified polynomial $\tilde{p}_{ij}(x, y)$ such that

$$\tilde{p}_{ij}(x,y) = \hat{\theta} p_{ij}(x,y) + (1-\hat{\theta})\overline{u}_{ij},$$
$$\hat{\theta} = \min\left(\left|\frac{M-\overline{u}_{ij}}{M_{ij}-\overline{u}_{ij}}\right|, \left|\frac{m^*-\overline{u}_{ij}}{m^*_{ij}-\overline{u}_{ij}}\right|, 1\right), \quad (28)$$

where the local extrema are $M_{ij} = \max[p_{ij}(x, y)]$ and $m^*_{ij} = \min[p_{ij}(x, y)]$. In (28) M and m^* are the global maximum and minimum values of the initial condition, respectively, which are usually known in the context of the transport of certain atmospheric tracers. From (28) it is clear that $\tilde{p}_{ij}(x, y)$ preserves the cell-average $\overline{u}_{ij}$, implying local conservation when $\hat{\theta} \in [0, 1]$. Note that the positivity-preserving option is a special case of the BP filter, and can be achieved by setting $m^* = 0$.

We tested the BP filter for SD advection using the cosine-bell test with the same configuration considered above. Figure 2b shows the SD numerical results with the BP filter after one revolution, where the solution is free of negative values, and the height of the bell is in the range of [0, 996.6] m. The mass error for this case is found to be within the order of machine precision, as expected.

c. Steady-state geostrophic flow

This is the steady-state test known as test case 2 in W92. Since the exact solution is known, this test provides an excellent tool for studying the convergence of the numerical solution. The wind field is uniform (non-divergent) and is the same as (26)–(27), defined for the solid-body rotation test. Here the nonlinear shallow-water equations are geostrophically balanced during the time evolution. The initial height field is defined as

$$gh = gh_0 - \left(R\omega u_0 + \frac{u_0^2}{2}\right) \times (\sin\theta\cos\alpha - \cos\lambda\cos\theta\sin\alpha)^2, \quad (29)$$

where $gh_0 = 2.94 \times 10^4\ \mathrm{m^2\,s^{-2}}$, ω is the angular velocity of the earth, and other parameters are as defined for the previous test case. The SW model is integrated for 5 model days as recommended in W92. Convergence of the ℓ_1 and ℓ_∞ height errors with the SD version of the SW model is shown in Fig. 4. Figure 4a shows the so-called p errors, obtained by keeping the total number of elements the same ($N_e = 3$), but varying the polynomial degree $N(=N_v - 1)$ from 4 to 10. We employ the third-order strong-stability-preserving Runge–Kutta (SSP-RK) time integration scheme (Gottlieb et al. 2001) for both variants of the SW model. The time step used for this test was $\Delta t = 180$ s, except for the case when $N = 10$, for which $\Delta t = 90$ s. Figure 4b shows the h errors obtained by fixing the degree of the polynomial $N = 3$ (i.e., using a 4×4 GLL grid and gradually varying the number of elements $N_e = 5, 7, \ldots, 15$). The convergence results with SD discretization is identical to that of the DG results (not shown), and consistent with the results reported in Bao et al. (2014). The p errors (Fig. 4a) show spectral convergence with the SD discretization while h errors indicate more than fourth-order convergence, which is consistent with the spatial order of accuracy of the SD discretization. The SD version of the SW model is found to be about 18% faster than the nodal DG model for this test.

d. Zonal flow over an isolated mountain

The last SW test we consider deals with a zonal flow over an isolated mountain, also known as the SW test case 5 in W92. Zonal flow is the same as in the steady-state flow described above [initial conditions in (26)–(29)]; however, a new set of parameters are chosen: $\alpha = 0$, $u_0 = 20\ \mathrm{m\,s^{-1}}$, and the mean equivalent depth of the atmosphere is set to be $h_0 = 5960$ m. The *mountain* is centered at $(\lambda_c, \theta_c) = (3\pi/2, \pi/6)$ with height $h_s = 2000(1 - r/a)$ m, where $a = \pi/9$ and $r^2 = \min[a^2, (\lambda - \lambda_c)^2 + (\theta - \theta_c)^2]$. For the SW test case 5, the flow field is highly nonlinear and no analytic solution is available. We use both DG and SD discretization of the SW equations with the same grid configurations (Fig. 2), and the time integration is performed with a third-order explicit SSP-RK method as in the previous test case. Figure 5a shows the numerical results for the height (m) field with SD after 15 days of model integration, with a time step of $\Delta t = 240$ s. A cubed-sphere grid with $12 \times 12 \times 6$ elements and the fourth-order SD scheme employing 4×4 GLL points on each element (Fig. 2a) are used for the simulation. Figure 5b shows the difference between the SD and DG solutions, which is negligibly small [$O(10^{-10})$ m]. For this test case, high-order methods such as the spectral-element method without spatial filtering introduce spurious oscillations (spectral ringing). However, as in the

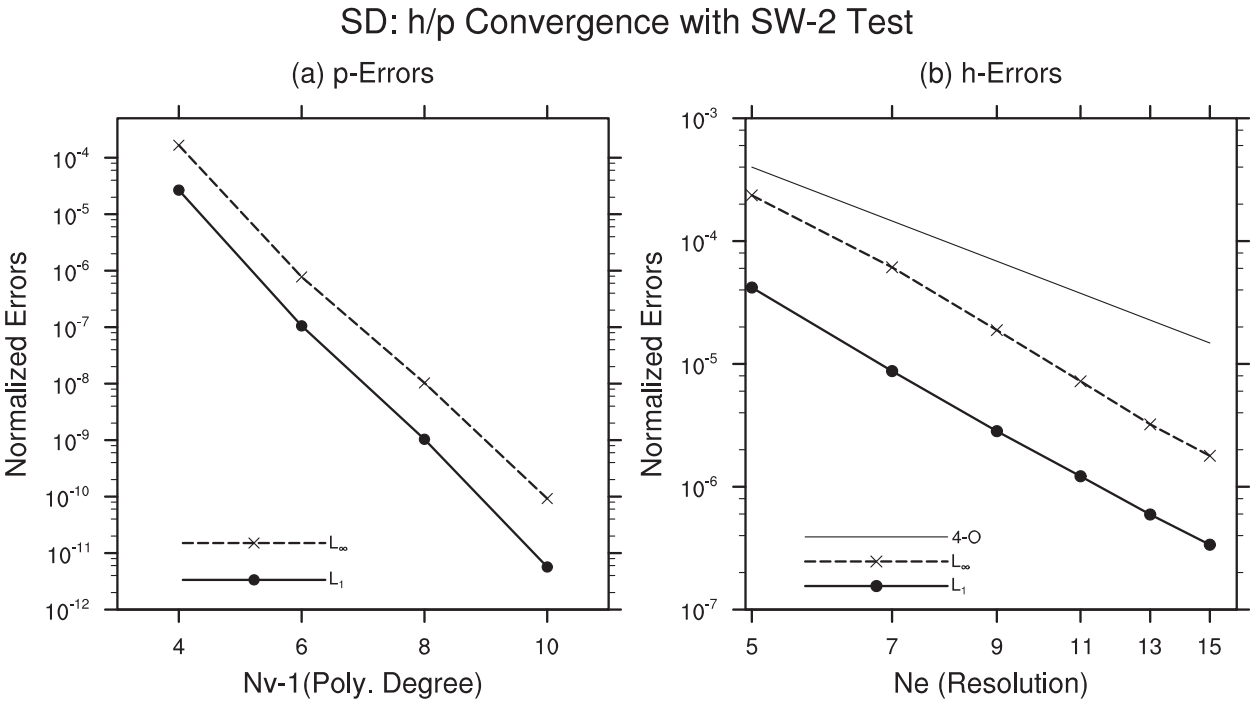

FIG. 4. Convergence of the ℓ_1 (solid line) and ℓ_∞ (dashed line) height errors for the SW test case 2 (geostrophic flow) after 5 days of simulation. (a) The p convergence where total number of elements fixed ($N_e = 3$) and the degree of the polynomial is gradually increased. (b) The h convergence where the degree of the polynomial is fixed ($N = N_v - 1 = 3$) and the number of elements (N_e) is increased.

case of the DG method (Nair et al. 2005), the SD solution is found to be smooth and free of spurious oscillation.

Next we consider the influence of the diffusion mechanism in the evolution of the relative vorticity (ζ) fields for the SD viscous SW model. A high-order version of the SD model is integrated for 10 model days with $N_e = 18$ and 6×6 GLL points on each element, which corresponds to 1° horizontal resolution at the equator. The diffusion coefficient $\nu = 2.5 \times 10^5\ \mathrm{m^2\ s^{-1}}$ is used for the viscous SW model. Vorticity fields are initially generated near the mountain and are well developed after a few days, spreading to the entire domain. Figures 6a and 6b show the SD results with $\nu = 0$ at model days 2 and 10, respectively. The inviscid solution at day 10 (Fig. 6b) shows some spurious oscillations and small-scale features. This noise is completely removed, as expected, for the viscous model results shown in Fig. 6c. The DG SW model discretizes the diffusion operator using the "BR2" scheme, which is a special case of LDG method (Nair 2009). For reference, the DG results with the same experimental setup are shown in Fig. 6d, which is visually identical to the corresponding SD results (Fig. 6c). Note that while the choice of diffusion coefficient ν is somewhat arbitrary, technically, it should be a resolution-(problem) dependent parameter. Nevertheless, our choice of ν is just for making a comparison of the SD viscous results as opposed to the DG results.

One of the motivating factors for considering the SD method is its inherent computational efficiency. In our implementation, we found that the quadrature-free version of the SW model is about 18% more efficient (faster) than the nodal DG version, for the same quality results. In addition, it is found that the SD viscous SW model is about 24% more efficient than the DG counterpart. For parallel implementation, the quadrature-free SD diffusion operator requires only one MPI communication per Laplacian evaluation because of the compact nature of the computational stencil. This is very promising for practical atmospheric models, which usually employ fourth-order (∇^4) hyperdiffusion, and the SD diffusion process can be seamlessly extended for this purpose.

4. Summary

Standard DG discretization relies on the integral (weak) form of the partial differential equations (PDE). This invariably introduces several surface and line integrals on each element in the discretization, which are evaluated by means of Gauss quadrature rules. The DG schemes are known to be very accurate at a high computational cost, partially due to the multiple integral evaluations in the discretization. The flux reconstruction (FR) approach of Huynh (2007) is a framework for high-order schemes including the quadrature-free DG method,

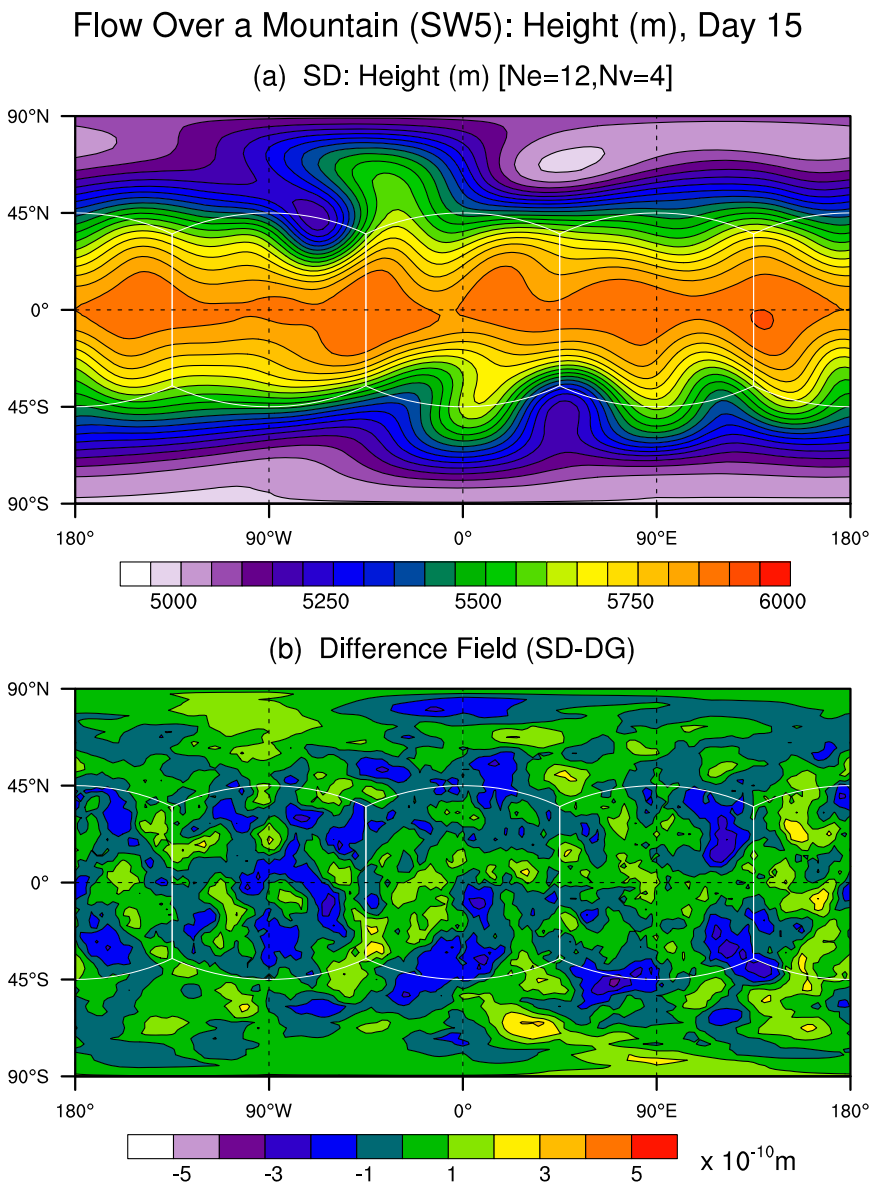

FIG. 5. (a) The simulated height field (m) with SD model for the SW test case 5 (flow over a mountain) at day 15. The model is integrated at an approximate resolution 2.5° ($N_e = 12$, $N_v = 4$) with a time step $\Delta t = 240$ s. (b) The difference of height filed (SD minus DG) from the results with the DG model, using the same model configuration.

and solves the equations in differential form by means of spectral differencing. A potential computational advantage of FR schemes is that the PDEs are directly discretized without volume or surface integrals. The flux correction functions in the FR approach correct fluxes at the element edges to maintain the continuity across element edges.

We have implemented the quadrature-free form of the DG method using the FR approach combined with spectral differencing (the SD method) for the shallow-water (SW) equations (both inviscid and viscous) on the cubed sphere, and its performance is compared with the regular nodal DG method. A bound (positivity) preserving local limiter is tested for the SD advection problem, which maintains the positivity of the solution without degrading the accuracy or conservation properties of the SD scheme. The error norms show that the results with both formulations are virtually identical; however, the quadrature-free formulation is about 18% more computationally efficient (faster) and is easy to implement. For the viscous SW model employing second-order diffusion, the SD model produces a visually

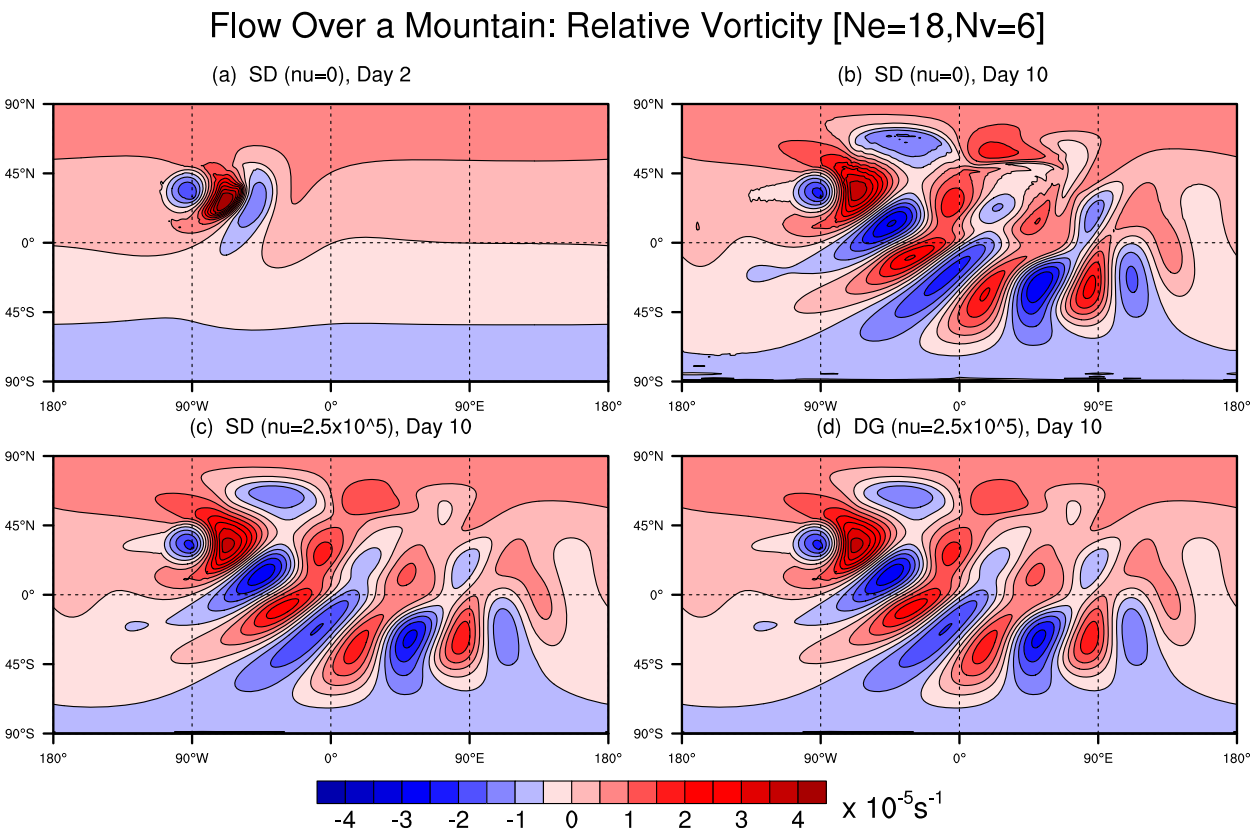

FIG. 6. The relative vorticity (ζ) fields for the SW test case of flow over an isolated mountain at an approximate horizontal resolution of 1° ($N_e = 18$, $N_v = 6$). (a) The SD SW results without diffusion at model day 2. (b) As in (a), but at day 10. (c) The SD results (viscous) with diffusion coefficient $\nu = 2.5 \times 10^5$ m^2 s^{-1} at day 10. (d) The reference solution with the DG SW model with the same experimental setup as in (c).

indistinguishable solution compared to the regular DG counterpart. Moreover, for the viscous case, the SD formulation is found be 24% more efficient. For a 3D atmospheric model (Nair et al. 2009), we anticipate the quadrature-free formulation will greatly improve efficiency, which is an ongoing research project.

Acknowledgments. The author would like to thank the anonymous reviewers for their constructive comments, which immensely helped to improve the manuscript. Thanks are due to Dr. Mike Toy and Lei Bao for an internal review of the manuscript, and the author would like to acknowledge Dr. H. T. Huynh for a helpful discussion.

REFERENCES

Allaneau, Y., and A. Jameson, 2011: Connections between the filtered discontinuous Galerkin method and the flux reconstruction approach to high-order discretizations. *Comput. Methods Appl. Mech. Eng.,* **200,** 3628–3636, doi:10.1016/j.cma.2011.08.019.

Arnold, D. N., F. Brezzi, B. Cockburn, and L. D. Marini, 2002: Unified analysis of discontinuous Galerkin methods for elliptic problems. *SIAM J. Numer. Anal.,* **39,** 1749–1779, doi:10.1137/S0036142901384162.

Atkins, H., and C.-W. Shu, 1998: Quadrature-free implementation of the discontinuous Galerkin method for hyperbolic equations. *AIAA J.,* **36,** 775–782, doi:10.2514/2.436.

Bao, L., R. D. Nair, and H. M. Tufo, 2014: A mass and momentum flux-form high-order discontinuous Galerkin shallow water model on the cubed-sphere. *J. Comput. Phys.,* **271,** 224–243, doi:10.1016/j.jcp.2013.11.033.

Bassi, F., and S. Rebay, 1997: A high-order accurate discontinuous finite element method for the numerical solution of the compressible Navier–Stokes equations. *J. Comput. Phys.,* **131,** 267–279, doi:10.1006/jcph.1996.5572.

Chen, C., and F. Xiao, 2008: Shallow water model on cubed-sphere by multi-moment finite volume method. *J. Comput. Phys.,* **227,** 5019–5044, doi:10.1016/j.jcp.2008.01.033.

Cockburn, B., 1997: An introduction to the Discontinuous-Galerkin method for convection-dominated problems. *Lecture Notes in Mathematics: Advanced Numerical Approximation of Nonlinear Hyperbolic Equations,* A. Quarteroni, Ed., Vol. 1697, Springer, 151–268.

——, and C.-W. Shu, 1998: The local discontinuous Galerkin for convection diffusion systems. *SIAM J. Numer. Anal.,* **35,** 2440–2463, doi:10.1137/S0036142997316712.

De Grazia, D., G. Mengaldo, D. Moxey, P. E. Vincent, and S. J. Sherwin, 2014: Connections between the discontinuous

Galerkin method and high-order flux reconstruction schemes. *Int. J. Numer. Methods Fluids,* **75,** 860–877, doi:10.1002/fld.3915.

Deville, M. O., P. F. Fisher, and E. M. Mund, 2002: *High-Order Methods for Incompressible Flow*. Cambridge University Press, 499 pp.

Gao, H., Z. J. Wang, and H. T. Huynh, 2013: Differential formulation of discontinuous Galerkin and related methods for the Navier–Stokes equations. *Commun. Comput. Phys.,* **13,** 1013–1044.

Giraldo, F., J. Hesthaven, and T. Warburton, 2002: Nodal high-order discontinuous Galerkin methods for spherical shallow water equations. *J. Comput. Phys.,* **181,** 499–525, doi:10.1006/jcph.2002.7139.

Gottlieb, S., C.-W. Shu, and E. Tadmor, 2001: Strong stability-preserving high-order time discretization methods. *SIAM Rev.,* **43,** 89–112, doi:10.1137/S003614450036757X.

Huynh, H. T., 2007: A flux reconstruction approach to high-order schemes including discontinuous Galerkin methods. AIAA Paper 2007-4079, *18th AIAA Computational Fluid Dynamics Conf.,* Miami, FL, AIAA, 1–42.

——, 2009: A reconstruction approach to high-order schemes including discontinuous Galerkin for diffusion. AIAA Paper 2009-403, *47th AIAA Aerospace Science Meeting,* Orlando, FL, AIAA, 1–34.

——, 2014: On formulation of discontinuous Galerkin and related methods for conservation laws. Tech. Note NASA/TM-2014-218135, NASA, 1–28.

Kopriva, D. A., and J. H. Kolias, 1996: A conservative staggered-grid Chebyshev multidomain method for compressible flows. *J. Comput. Phys.,* **125,** 244–261, doi:10.1006/jcph.1996.0091.

Liang, C., C. Cox, and M. Plesniak, 2013: A comparison of computational efficiencies of spectral difference method and correction procedure via reconstruction. *J. Comput. Phys.,* **239,** 138–146, doi:10.1016/j.jcp.2013.01.001.

May, G., 2011: On the connection between the spectral difference method and the discontinuous Galerkin method. *Commun. Comput. Phys.,* **9,** 1071–1080.

Nair, R. D., 2009: Diffusion experiments with a global Discontinuous Galerkin shallow-water model. *Mon. Wea. Rev.,* **137,** 3339–3350, doi:10.1175/2009MWR2843.1.

——, S. J. Thomas, and R. D. Loft, 2005: A discontinuous Galerkin global shallow water model. *Mon. Wea. Rev.,* **133,** 876–888, doi:10.1175/MWR2903.1.

——, H.-W. Choi, and H. M. Tufo, 2009: Computational aspects of a scalable high-order discontinuous Galerkin atmospheric dynamical core. *Comput. Fluids,* **38,** 309–319, doi:10.1016/j.compfluid.2008.04.006.

——, M. N. Levy, and P. H. Lauritzen, 2011: Emerging numerical methods for atmospheric modeling. *Numerical Techniques for Global Atmospheric Models,* P. H. Lauritzen et al., Eds., Vol. 80, Springer-Verlag, 189–250.

Sadourny, R., 1972: Conservative finite-difference approximations of the primitive equations on quasi-uniform spherical grids. *Mon. Wea. Rev.,* **100,** 136–144, doi:10.1175/1520-0493(1972)100<0136:CFAOTP>2.3.CO;2.

Williamson, D., J. Drake, J. Hack, R. Jacob, and P. Swarztrauber, 1992: A standard test set for numerical approximations to the shallow water equations in spherical geometry. *J. Comput. Phys.,* **102,** 211–224, doi:10.1016/S0021-9991(05)80016-6.

Zhang, X., and C.-W. Shu, 2010: On maximum-principle-satisfying high order schemes for scalar conservation laws. *J. Comput. Phys.,* **229,** 3091–3120, doi:10.1016/j.jcp.2009.12.030.

Zhang, Y., and R. D. Nair, 2012: A nonoscillatory discontinuous Galerkin transport scheme on the cubed sphere. *Mon. Wea. Rev.,* **140,** 3106–3126, doi:10.1175/MWR-D-11-00287.1.